ChemSusChem

Chemistry Europe
European Chemical Societies Publishing
ChemSusChem

RESEARCH ARTICLE OPEN ACCESS

Decoding Fluorine Peripheral Substitution Impact in Zinc Phthalocyanines for Perovskite Solar Cells

Son Singh[1] | Adrián Hernández[2] | Javier Ortiz[2] | Samrana Kazim[3,4] | Luis Lezama[5] | Eliseo Ruiz[6] | Ángela Sastre-Santos[2] | Shahzada Ahmad[1,7]

[1]BCMaterials, Basque Center for Materials, Applications, and Nanostructures, Leioa, Spain | [2]Área de Química Orgánica, Instituto de Bioingeniería, Universidad Miguel Hernández, Elche, Spain | [3]Aragón Institute of Engineering Research (I3A), Universidad de Zaragoza, Zaragoza, Spain | [4]Aragonese Foundation for Research and Development (ARAID), Government of Aragon, Zaragoza, Spain | [5]Departamento de Química Inorgánica, Facultad de Ciencia y Tecnología, Universidad del País Vasco, Leioa, Spain | [6]Departament de Química Inorgànica i Orgànica, and Institut de Química Teòrica i Computacional, Universitat de Barcelona, Barcelona, Spain | [7]IKERBASQUE, Basque Foundation for Science, Bilbao, Spain

Correspondence: Ángela Sastre-Santos (asastre@umh.es) | Shahzada Ahmad (shahzada.ahmad@bcmaterials.net)

Received: 11 September 2025 | **Revised:** 24 November 2025 | **Accepted:** 30 November 2025

Keywords: Density Functional Theory calculations | Trifluoroethoxy arm | hole transport materials | perovskite solar cells | phthalocyanines

ABSTRACT

We designed six zinc phthalocyanine derivatives (ZnPc-1–ZnPc-6) as molecular semiconductors. By adjusting peripheral substituents with differing electron-donating and -withdrawing properties ($-C(CH_3)_3$, $-O(CH_2)CF_3$, $-CF_3$), we rationalized solubility, energy levels, and molecular arrangement to influence interfacial charge dynamics and thus device performance. Among the derivatives, **ZnPc-2** with three *tert*-butyl groups and a trifluoroethoxy provides favorable energy level alignment, better thin film coverage, and high conductivity suited to be used as hole-selective materials. When integrated into n–i–p architecture perovskite solar cells, it measures a power conversion efficiency approaches that of Spiro-OMeTAD under our lab conditions. **ZnPc-2** showed ambient operational stability, maintaining around 80% of its initial J_{MPP} over 24 h without encapsulation. Our combined theoretical and experimental assessment revealed detailed electro-optical properties to substantiate the influence of molecule design on the device performance. Specifically, three *tert*-butyl groups with a trifluoroethoxy arm outperform, evidencing molecular design as a strategy to modulate properties.

1 | Introduction

Halide perovskite solar cells (PSCs) have progressed as an upcoming photovoltaics technology due to their unparalleled power conversion efficiency (PCE), lower production costs that will allow achieving a lower energy payback time than silicon photovoltaics [1–5]. However, attaining enduring operational stability continues to pose a hurdle for their full exploitation. Typically, PSCs entail an electron transporting layer (ETLs), where a perovskite active layer is sandwiched with a hole transport material (HTMs). The choice of HTMs influences the long-term stability of PSCs not only by reducing recombination losses [6] but also by resisting the photo-degradation pathways. In this vein, a wide range of small-molecule and polymer-based HTMs are being investigated [7–13]. In advanced n–i–p architecture PSCs, the organic hole transport layer is commonly 2,2′,7,7′-tetrakis(*N*, *N*-di-p-methoxyphenylamine)-9,9′-spirobifluorene (Spiro-OMeTAD). Spiro-OMeTAD needs chemical p-doping with lithium bis(trifluoromethanesulfonyl)imide (LiTFSI) and 4-*tert*-butylpyridine (*t*-BP) to achieve adequate conductivity; further, this is plagued by the intricate synthesis procedures and purification processes of Spiro-OMeTAD [14, 15]. Strategies to address these challenges entail the development of alternative, cost-effective, and reliable HTMs, including thermal stability in the presence of additives.

Son Singh and Adrián Hernández contributed equally to this study.

Phthalocyanines (Pcs), which are structurally resembling porphyrins, represent a category of resilient p-type organic semiconductors that are attractive as HTMs in the n–i–p architecture PSCs due to their distinctive attributes, including moisture, thermal, and chemical stability [16–18], which arises from their organic–inorganic nature. Transition metal phthalocyanine complexes (MPcs) have been explored as HTMs in PSCs, including copper phthalocyanines (CuPc), nickel phthalocyanines (NiPcs), and zinc phthalocyanines (ZnPcs). Furthermore, the replacement of metals in phthalocyanines, whether with nonperipheral or peripheral substituents, is key in tuning the electro-optical characteristics of MPcs, for energy levels tuning and identifying solubility in conventional solvents [19–22]. CuPc-based PSCsmeasured a PCE of ~18% and preserved 97% of their initial performance after 1000 h at 85°C [23]. Using solution-processed CuPc with a post-treatment, the PSCs registered >20% PCE with thermal and light stability (no visible degradation after 2000 h at 85°C) [24]. NiPc, when substituted with four methoxyethoxy groups, showed stability in moisture, heat, and light [21]. These findings highlight the potential of phthalocyanine derivatives to induce reliability.

The electronic characteristics of ZnPc derivatives can be modulated with peripheral substituents, and their highest occupied molecular orbital (HOMO) levels, which are typically deeper, can align well with perovskite valence bands, making them a rational choice. Recent studies investigated ZnPc dimers, diarylamine ZnPcs, and a series of *tert*-butyl-substituted ZnPc molecules in PSCs, reporting improved ambient stability comparable to Spiro-OMeTAD [25–27]. Conceivably, these findings suggest that with rational molecular design, ZnPc-based HTMs are potentially attractive candidates. However, there are still challenges associated with determining the effective ZnPc structures and comprehending how they interact with the perovskite layer. Arguably, fluorinated molecular semiconductors can induce high hydrophobicity and rational molecular packing, which in turn will boost the hole mobility and conductivity. Fluorinated Spiro-OMeTAD with a PCE of 24.8% was reported, and this high PCE is ascribed to lower energy levels in the fluorinated molecules, along with high molecular packing [28, 29].

We developed six new Zn(II) phthalocyanine derivatives, designated as ZnPc-1–ZnPc-6, to assess their suitability in PSCs. We synthesized a series of ZnPc related derivatives with substitutions at the β-position, including four *tert*-butyl groups (**ZnPc-1**) as reference, one trifluoroethoxy group (**ZnPc-2**), four trifluoroethoxy groups (**ZnPc-3**), one trifluoromethyl group (**ZnPc-4**), three trifluoromethyl groups (**ZnPc-5**), and four trifluoromethyl groups (**ZnPc-6**), to deduce their impact of structural variations on photophysical properties, charge transport, and device performance. Benchmark devices using Spiro-OMeTAD were made for comparative analysis. We noted among this series, **ZnPc-2** facilitates effective device performance, attaining efficiency inching toward Spiro-OMeTAD, and with enhanced operational stability. Our findings underscore **ZnPc-2** as an effective material that resolves the stability concerns associated with Spiro-OMeTAD while delivering competitive performance.

2 | Results and Discussion

2.1 | Synthesis of ZnPcs

Zinc phthalocyanine (ZnPc) and its derivatives, owing to their extensive π-conjugated core, show exceptional thermal and chemical durability and adaptable electronic characteristics based on their structural variations. We synthesized and investigated six ZnPc derivatives with distinct terminal substituents—*tert*-butyl ($-C(CH_3)_3$), trifluoroethoxy ($-O(CH_2)CF_3$), and trifluoromethyl ($-CF_3$)—assessing their efficacy as hole transport (Figure 1a).

Phthalonitriles **7**, **8**, and **ZnPc-1** are synthesized accordingly [30–32], while Phthalonitrile **9** is commercially available. Synthesis of **ZnPc-3** and **ZnPc-6** is carried out by cyclotetramerization of the

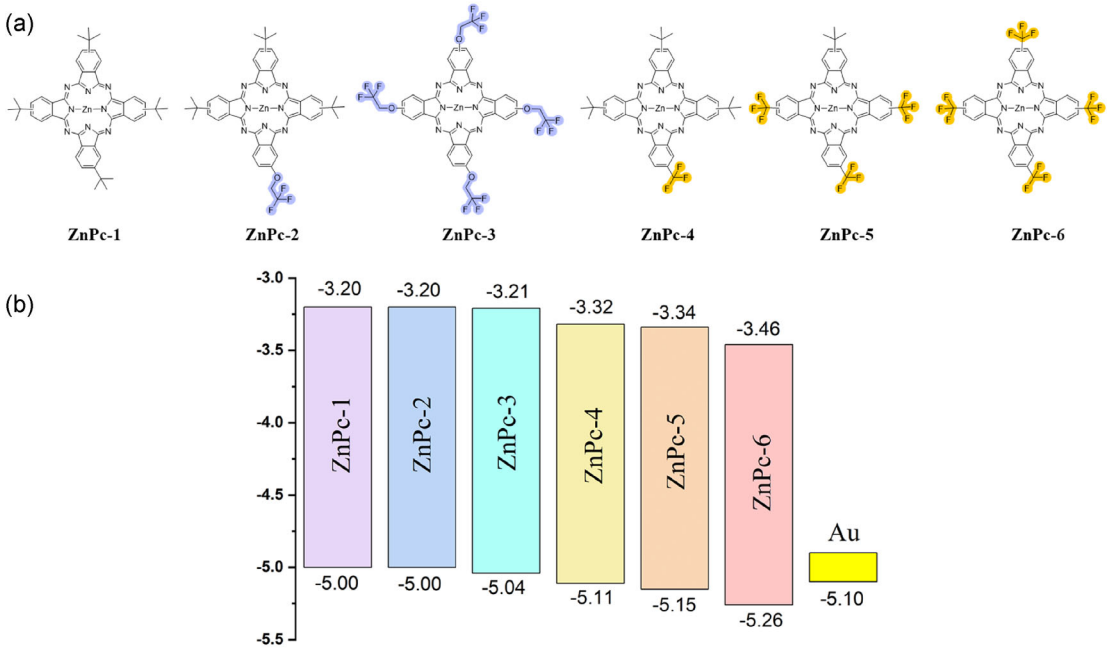

FIGURE 1 | (a) Molecular structures of zinc phthalocyanine (ZnPc) derivatives (**ZnPc-1–6**) and (b) energy-level diagram illustrating the HOMO and LUMO values.

corresponding phthalonitrile (**7** or **8**) and $Zn(OAc)_2$, with a yield of 54% and 46%, respectively, after purification. The synthesis of asymmetrical MPcs is carried out by statistical cyclotetramerization between the appropriate phthalonitrile **7** or **8**, phthalonitrile **9,** and zinc acetate. After purification by column chromatography, **ZnPc-2**, **ZnPc-4**, and **ZnPc-5** are obtained with 6%, 15%, and 12% yield, respectively (Scheme 1). All ZnPcs are obtained as a mixture of regioisomers and fully characterized by proton nuclear magnetic resonance (^{1}H-NMR), fluorine nuclear magnetic resonance (^{19}F-NMR), high-resolution-matrix-assisted laser desorption ionization time-of-flight mass spectrometry (HR-MALDI-ToF), UV–vis absorption spectroscopy, fluorescence emission spectroscopy, and fourier transform infrared spectroscopy (FT-IR) (SI and experimental section).

The ^{1}H-NMR spectra of ZnPc in THF-d_8 showed well-defined aromatic and aliphatic signals. All compounds exhibit signals in the aromatic region corresponding to the 12 protons of the isoindole units of the phthalocyanine core. For **ZnPc-2**, five distinct signals between 9.59 and 7.87 ppm account for these twelve protons, while two additional signals appear at 5.18 ppm (2H) and 1.81 ppm (27H), attributed to methylene protons of the side chain and the methyl groups of three *tert*-butyl substituents, respectively (Figure S1). In contrast, the symmetric **ZnPc-3** shows only three aromatic signals between 9.08 and 7.68 ppm for the twelve isoindole protons, a single signal at 5.15 ppm integrating for eight methylene protons (Figure S2). **ZnPc-4** displays five aromatic signals attributed to isoindole units between 9.66 and 8.29 ppm and a single aliphatic signal at 1.81 ppm integrating for 27 protons, corresponding to three *tert*-butyl groups (Figure S3). In **ZnPc-5**, the aromatic region (9.47–8.28 ppm) similarly integrates for twelve protons, but the aliphatic signal corresponds only to 9 protons, indicating the presence of a single tert-butyl group (Figure S4). Finally, the spectrum of **ZnPc-6** shows exclusively three signals between 9.41 and 8.39 ppm, integrating for twelve protons of the phthalocyanine core, in agreement with a highly symmetric structure bearing no aliphatic or side-chain protons (Figure S5). The progressive disappearance of signals in the aliphatic region across the series supports the controlled synthesis and purification of the synthesized derivatives. The ^{19}F-NMR spectra obtained for the series of ZnPc derivatives reveal characteristic chemical shifts that allow differentiation between distinct electronic environments of the fluorine atoms. In particular, **ZnPc-2** and **ZnPc-3** display signals in the ranges of −74.68 to −74.58 ppm and −74.61 to −74.49 ppm, respectively, and exhibit coupling with the protons of the adjacent methylene group. In contrast, compounds **ZnPc-4**, **ZnPc-5**, and **ZnPc-6** show more de-shielded signals, in the ranges of −61.43 to −61.25 ppm, −61.47 to −61.27 ppm, and −61.56 to −61.46 ppm, respectively, with no observable proton coupling (Figures S6 and S7).

2.2 | Electro-Optical and Physical Properties

The UV–vis absorption spectra of the **ZnPcs 1–6** measured in DMF as solvent display the characteristic Soret and Q bands, appearing around 350 nm and between 600–780 nm, respectively (Figure 2). The UV–vis absorption spectra exhibit pronounced variations in both the intensity and position of the B and Q bands, and these spectral differences correlate closely with the identity and number of peripheral substituents. **ZnPc-1** and **ZnPc-2** show the highest absorption intensities in both bands, suggesting enhanced conjugation and solubility due to the presence of multiple *tert*-butyl groups. **ZnPc-3** displays slightly broader and less intense absorption, possibly due to increased substitution symmetry and reduced steric hindrance. Even though **ZnPc-4** also bears three *tert*-butyl groups, it displays a notably lower absorption intensity, likely due to the presence of a $-CF_3$ group—a strongly electron-withdrawing substituent

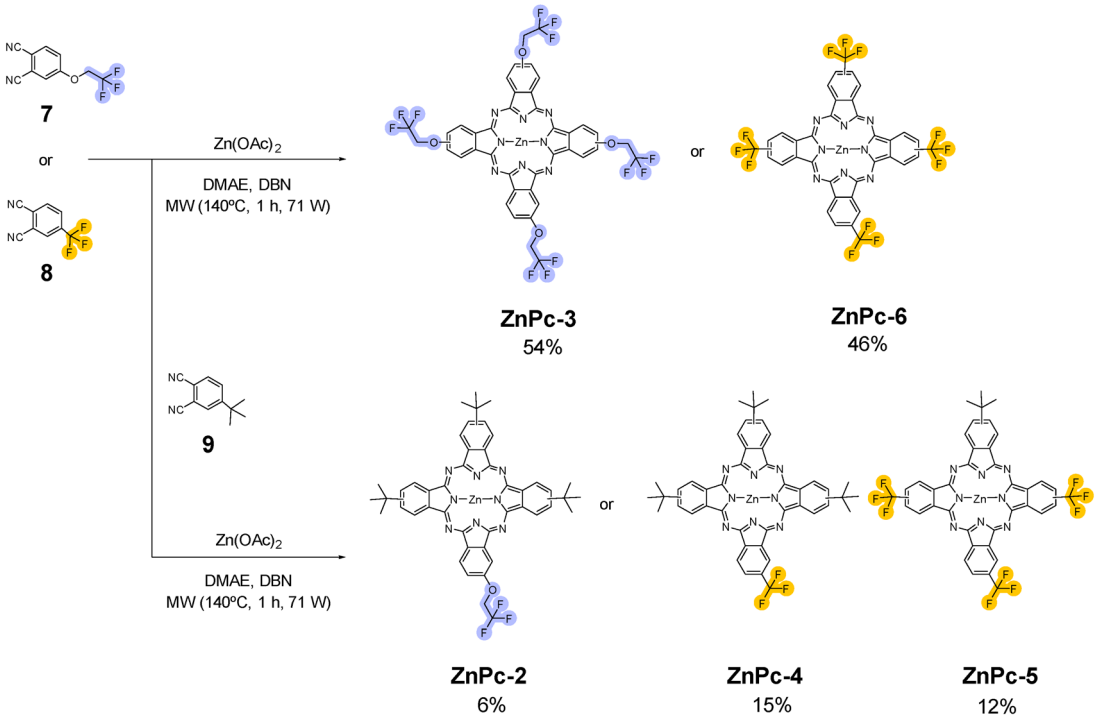

SCHEME 1 | Synthetic Route of **ZnPcs 2–6**.

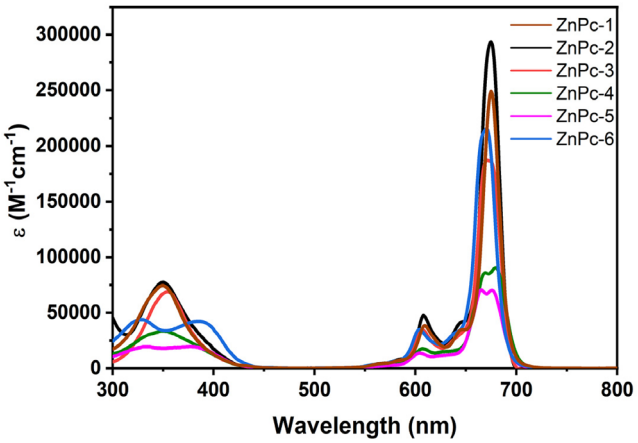

FIGURE 2 | UV–Vis absorption spectra of zinc phthalocyanines **1–6** in DMF.

—directly attached to the aromatic ring. The Q bands of **ZnPc-4** and **ZnPc-5** exhibit distinct splitting around 690 nm, which is attributed to the perturbation of the electronic structure due to the asymmetric character of these systems. Likewise, **ZnPc-5 and ZnPc-6** show a clear splitting in the B-band around 350 nm, ascribed to a charge transfer from the CF_3 to the ZnPc core. Notably, even subtle modifications in the substituent identity and number can considerably affect the optical properties of phthalocyanine chromophores.

We carried out electrochemical characterization using cyclic voltammetry in dry DMF as solvent, with ferrocene serving as an external standard (Figure S8) to determine the energy level of the HOMO (E_{HOMO}) using the equation: $E_{HOMO} = -4.8 - E_{Ox1}$, where E_{Ox1} represents the first oxidation potential. The energy level of the lowest unoccupied molecular orbital (E_{LUMO}) is calculated by adding the optical band gap to the E_{HOMO} value. Fluorescence emission spectra of the ZnPc derivatives are recorded by exciting at the wavelength corresponding to their respective Q-band absorption maxima (Figures S9–S14). The optical band gap for each compound is estimated from the intersection point of the normalized absorption and emission spectra. To complement our results, Density Functional Theory (DFT) calculations are also performed, to obtain energy level values, (Table 1). Both the experimental and computed results are in agreement; however, due to the similarity in **ZnPcs 1–6** compounds, it is difficult to precisely extract a clear difference. Though the influence of the ligands on the HOMO and LUMO levels is more significant.

Tert-butyl-substituted ZnPcs possess four connected $-C(CH_3)_3$ groups and exhibit mild electron-donating properties through hyperconjugation and are notably bulky. *Tert*-butyl substituents elevate the HOMO marginally (in comparison to electron-withdrawing groups) and mostly function to enhance solubility and inhibit aggregation of ZnPc molecules. Such behavior of the HOMO is also established by the DFT calculations. ZnPc derivatives with 1–4 *tert*-butyl groups suggest that the fully substituted ZnPc (ZnPc–4*t*Bu) produces a homogeneous, granular thin film suitable as an HTM [27]. Trifluoroethoxy-substituted zinc phthalocyanine possesses $-O(CH_2)CF_3$ groups in its perimeter. The $O(CH_2)CF_3$ moiety features a methoxy bridge connecting the aromatic ring to the CF_3 group. This group exhibits a significant electron donor capacity due to the $O-(CH_2)-$, which is compensated by the electron-withdrawing character of the CF_3 because the inductive effect still transmits through the sigma bonds and possesses a marginally greater steric bulk owing to the methoxy connection. This dual behavior of the $-O(CH_2)CF_3$ group is clearly shown in the electrostatic potential maps (Figure 3), the $-CF_3$ group also generates electropositive and electronegative regions, although these are less pronounced, while 1–4 *tert*-butyl groups generate just a weak electropositive area. We anticipate the $-O(CH_2)CF_3$ substituents to decrease the HOMO energy (less than CF_3) while perhaps interrupting π–π stacking to a larger extent (the oxygen can induce a minor twist or increase the distance between adjacent macrocycles). The $-O(CH_2)CF_3$ groups impart significant electronegativity and hydrophobicity, thus improving the moisture resistance of the HTM layers, while their steric dimensions may mitigate excessive aggregation of the ZnPc molecules in thin films. ZnPcs replaced with trifluoromethyl groups exhibit $-CF_3$ moieties at their perimeter. The $-CF_3$ group is a potent electron-withdrawing substituent, which markedly reduces the energy level of the highest occupied molecular orbital (HOMO) of ZnPc. Enhanced HOMO can optimize energy alignment with perovskite. The CF_3 substituents are small yet extremely electronegative, conferring hydrophobic properties to the molecule and will impact molecular arrangement in the solid phase (Figure 1b).

Despite the advantageous properties of ZnPc derivatives , the solubility of HTMs in chlorobenzene or dichlorobenzene (common HTM solvents) is a critical factor. Metal phthalocyanines with peripheral and nonperipheral substituents alter solubility in typical organic solvents, and noncovalent interaction among molecules promotes aggregation and reduces solubility in the majority of solvents (chlorobenzene, dichlorobenzene, toluene) [33, 34]. We noted **ZnPc-1**, **ZnPc-2**, and **ZnPc-4** hold good solubility

TABLE 1 | Electro-optical properties of ZnPcs 1–6 and in parentheses the DFT calculated values using TPSSh functional and 6-311G* (see computational details section).

Compound	E_{Red1}	E_{Ox1}	E_{LUMO}, eV	E_{HOMO}, eV	$E_{g\ Opt}$, eV	IP, eV	Dipolar moment
ZnPc-1	−1.37	0.20	−3.20 (−2.99)	−5.00 (−4.81)	1.80 (1.82)	5.92	0.6014
ZnPc-2	−1.34	0.20	−3.20 (−3.06)	−5.00 (−4.87)	1.80 (1.81)	5.98	2.3519
ZnPc-3	−1.31	0.24	−3.21 (−3.30)	−5.04 (−5.07)	1.83 (1.78)	6.16	3.1914
ZnPc-4	−1.48	0.31	−3.32 (−3.23)	−5.1 (−5.03)	1.79 (1.80)	6.16	4.6669
ZnPc-5	−1.13	0.35	−3.34 (−3.67)	−5.15 (−5.48)	1.81 (1.81)	6.62	7.3824
ZnPc-6	−1.15	0.46	−3.46 (−3.86)	−5.26 (−5.71)	1.80 (1.85)	6.87	3.1936

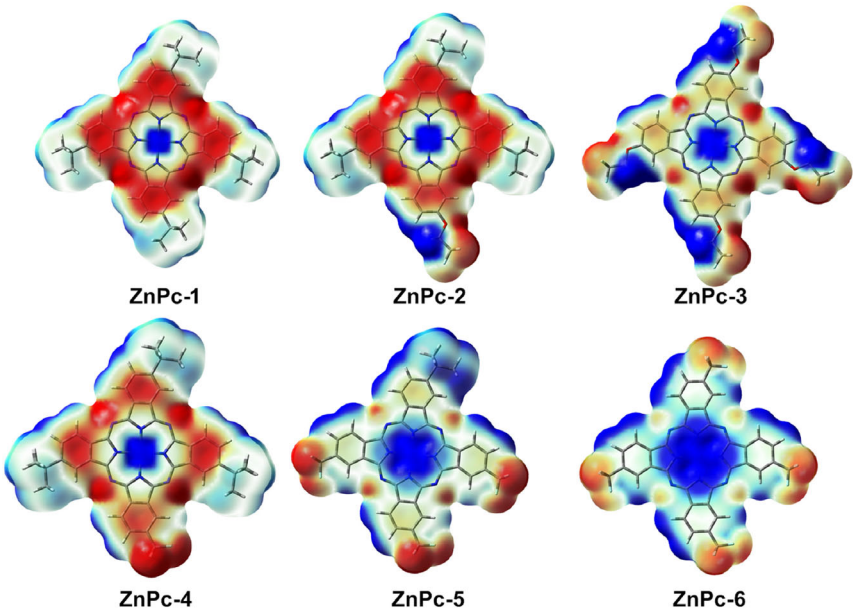

FIGURE 3 | DFT Calculated electrostatic potential maps projected on the electron density of zinc phthalocyanines **1–6**. All maps used consistent surface potential ranges, −0.015 a.u. (red) to 0.015 a.u. (blue), and an isovalue of 0.0004 e^-/bohr^3. Here, isovalue is the cutoff electron density from the molecular calculations used to define the outer boundary of the molecule.

in chlorobenzene, attributed to the presence of solubilizing substituents. In contrast, a reduction in the number of *tert*-butyl groups, as in **ZnPc-3**, **ZnPc-5**, and **ZnPc-6,** led to a noticeable decrease in solubility. To increase the solubility of the ZnPc derivatives, we discovered that a small amount of the more polar solvent tetrahydrofuran (THF) could be added to chlorobenzene. Figure S21 shows the solubility of ZnPcs in chlorobenzene and THF solvents.

The steady-state photoluminescence (PL) spectra of perovskite thin films on glass substrates with and without **ZnPcs 1–6** are measured with the excitation of 470 nm (Figure 4). The perovskite thin film has a strong emission peak centered at about 810 nm, ascribed to its inherent radiative recombination. On introducing ZnPcs atop it, the PL spectra are quenched, signifying that charge is being efficiently extracted at the perovskite/HTM interface.

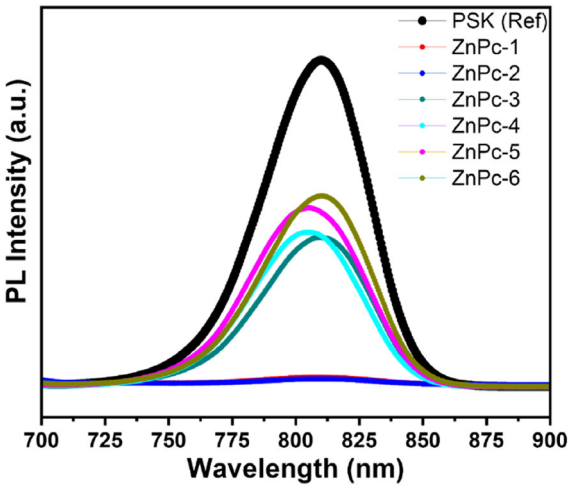

FIGURE 4 | Steady-state PL spectra of pristine perovskite films and perovskite coated with various ZnPc HTMs: **ZnPc-1** to **ZnPc-6**.

Among the ZnPc derivatives, **ZnPc-1** and **ZnPc-2** show significant PL emission quenching, implying effective hole extraction and interfacial charge transfer characteristics. This strong quenching suggests the energy levels of the perovskite valence band and the HOMO levels of ZnPc derivatives are aligned to allow hole injection and slow down carrier recombination. This was followed by **ZnPc-3** and **ZnPc-4,** which show a substantial decrease in PL intensity, advocating competitive hole extraction, but with minor restrictions, which could be due to poor interfacial morphology. In contrast, **ZnPc-5** and especially **ZnPc-6** show significantly less PL quenching; this minimal quenching indicates a lower hole extraction efficiency and higher interfacial recombination. We hypothesize this stems from poor thin film coverage and molecular packing, which all impede efficient charge transfer at the perovskite/HTM interface. The PL quenching follows the order of **ZnPc-1** ≈, **ZnPc-2** > **ZnPc-3** ≈, **ZnPc-4** > **ZnPc-5** > **ZnPc-6**. Our results underscore the value of design engineering in these ZnPc that significantly impact distinct hole-extraction abilities and interfacial characteristics.

For optimal device performance, as a prerequisite, the HTM should provide uniform coverage to the perovskite while preserving its morphology. We employed SEM (scanning electron microscopy) technique to investigate the surface microstructure of perovskite thin films after introducing HTMs. The top-view surface images of perovskite with varying HTM layers (Figure 5a–f), unfold **ZnPc-1** and **ZnPc-2** as a smooth and conformal surface morphology to the underlying perovskite grains. The **ZnPc-1** and **ZnPc-2** deposited thin films retain the compact granular morphology of the underlying perovskite, revealing a homogeneous coating without affecting the perovskite underneath. In contrast, other ZnPc derivatives induce apparent morphological alterations. **ZnPc-4** have a fibrillar or rough texture, indicating that **ZnPc-4** molecules aggregate differently or interact with the perovskite surface, promoting an uneven coating. While **ZnPc-5** and **ZnPc-6** exhibit partial coverage in some areas,

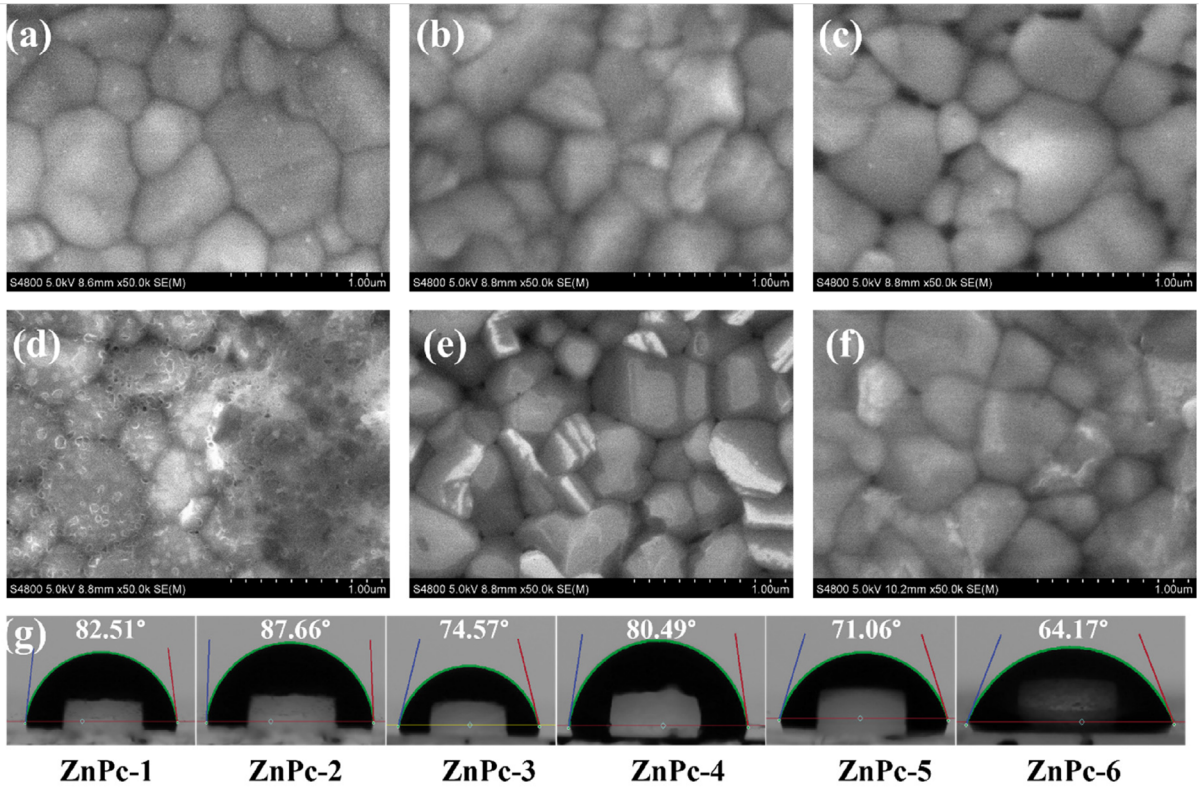

FIGURE 5 | SEM images show the surface morphology of perovskite thin films coated with different ZnPc derivatives: (a) **ZnPc-1**, (b) **ZnPc-2**, (c) **ZnPc-3**, (d) **ZnPc-4**, (e) **ZnPc-5**, and (f) **ZnPc-6** (scale bar: 1 μm), and (g) corresponding water contact angle measurements illustrating the surface wettability variations induced by the different ZnPc layers.

with grain boundaries or voids visible as dark lines or pinhole-like spots. An incomplete or inhomogeneous covering can result in shunting channels or inhibit hole collection. **ZnPc-1** and **ZnPc-2** have an advantageous properties in the ZnPc series; they resemble the Spiro layer in terms of homogeneous coverage, with no visible pinholes or large aggregates. This will be favourable for charge transfer as a smooth HTM/perovskite interface allows for rapid and homogenous hole extraction. The morphological findings are consistent with previous research that has shown how changing substituents on ZnPc molecules affects thin film microstructure (from granular to fibrous textures) [27]. This is also supported by surface wettability, as a uniform overlayer gave a higher contact angle value, and **ZnPc-2** showed the highest among them. We probed the wettability by measuring the static contact angles, which are also known as apparent angles. Notably, ZnPc-6 displays the lowest contact angle, even with the presence of CF_3 groups. SEM images, in both cross-sectional and surface topography, reveal that ZnPc-6 forms the thinnest (18 nm) and least conformal layer, with pinholes. Subsequently, the water droplet will wet a surface made up of both the HTM and the exposed perovskite. This lowers the apparent contact angle due to Cassie–Baxter mixing. Furthermore, the faceted microtexture of ZnPc-6 likely enhances its inherent wettability, a phenomenon known as the Wenzel effect. Moreover, the outermost surface might not be terminated with CF_3 groups due to molecular orientation, which would decrease the presence of CF_3 at the air interface. Therefore, the contact angle mostly reflects how much of the surface is covered and how the molecules are arranged, rather than just the type of molecules present. This is consistent with the observed reduced PL quenching.

X-band electron paramagnetic resonance (EPR) measurements made at room temperature revealed well-defined isotropic signals without any doping (Figure 6). The g-factor values closely match the value of a free electron (2.0023) across all ZnPcs. The spectra were fitted considering two contributions with different 'peak-to-peak' linewidths. We calculated the number of

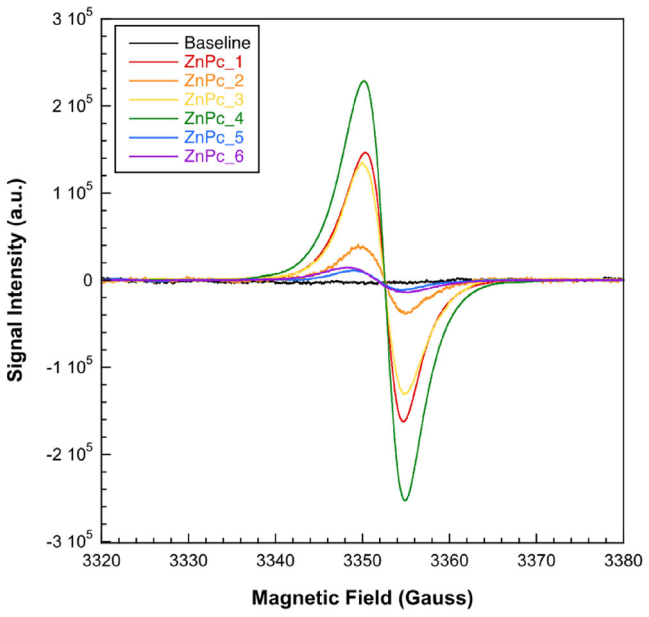

FIGURE 6 | Room-temperature EPR spectra acquired on solid ZnPcs 1–6.

unpaired spins per milligram in each ZnPc (Table 2) by referencing the EPR signal intensities with a copper sulfate standard. In all cases, the signal was fitted considering two contributions with different 'peak-to-peak' linewidths. ZnPc-4, followed by ZnPc-1, showed a higher concentration of unpaired electrons or holes compared to the other ZnPcs. To mention here, the measurements are carried out on solid samples, synthesized as such. This variation in design engineering adjusts the local electronic environment and modulates spin density distribution within the ZnPc molecules.

The charge transport properties of ZnPc are examined by assessing their conductivity and mobility values. The dark *I–V* characteristics of the devices with the configuration of ITO/HTM/Ag for **ZnPc-1** to **ZnPc-6**, demonstrating linear (ohmic) behavior as shown in Figure 7a. The slope of each curve reflects conductance, and the conductivity (σ) is retrieved using $\sigma = (I/VA)d$, where d is the HTM thickness and A is the active area of the devices [35]. The mean thickness of HTM is determined from the cross-sectional image of the devices (Figure S22). The conductivity value of **ZnPcs 1–6** derivatives is summarized (Table S1). **ZnPc-2** showed the highest σ, around 2×10^{-5} S·cm^{-1}, followed by the **ZnPc-1** and **ZnPc-4**, around 1.57×10^{-5} and 1.24×10^{-5} S·cm^{-1}. The remaining ZnPcs (**ZnPc-3**, **ZnPc-5**, and **ZnPc-6**) have lower conductivities, implying that all members of the series are comparable in charge-transport ability within an order of magnitude (Table S1). The trend indicates that electron-withdrawing fluoro substituents improve dark conductance, which is consistent with a larger inherent charge-carrier concentration or enhanced molecular packing in fluorinated derivatives.

The *J–V* curves (log-linear scale) for hole-only devices with the configuration of ITO/PEDOT:PSS/HTM/Ag are used to extract SCLC mobility (Figure 7b). At increasing bias, currents enter a space-charge-limited (trap-free) zone, with $J \propto V^2$. We used the Mott–Gurney equation for trap-free SCLC to determine the hole mobilities (μ_h) of each ZnPc HTM [36, 37].

$$J = 9\,\varepsilon_r\,\varepsilon_0\,\mu_h\,{V_{app}}^2/8L^3$$

where ε_r denotes the relative permittivity of the HTM (dielectric constant, presumed to be 3 for organic materials), ε_0 represents the permittivity of free space (8.85×10^{-12} F m^{-1}), μ_h represents the hole mobility of the HTM, V_{app} indicates the applied voltage, and L refers to the thickness of the HTM layers (Figure S22). The calculated hole mobility (μ_h) values range roughly two orders of magnitude (from ~10^{-6} to 10^{-4} cm^2/Vs), as summarized in Table S1, indicating a considerable dependency on molecule structure. **ZnPc-2** has the highest hole mobility of 2.75×10^{-4} cm^2/V·s, indicating relatively easy hole transport. **ZnPc-1** exhibits a substantial μ_h of 2.48×10^{-4} cm^2/V·s, which is comparable to **ZnPc-2**. The other ZnPc derivatives (**ZnPc-3**, **ZnPc-4**, and **ZnPc-5**) have intermediate mobilities on the order of 10^{-5} cm^2/Vs. The symmetric derivative **ZnPc-6** has the lowest hole mobility in the series.

The PSCs are developed using ZnPc 1–6, in a configuration as FTO/c-TiO_2/SnO_2/CsFAMAPbI_3/HTM/Au (Figure 8a), and their photovoltaic performance parameters under one-sun illumination is assessed to investigate the influence of the substituted organic moieties on performance. The ZnPc is spin-coated, and the concentration is kept at 10 mM as compared to 70 Mm of Spiro-OMeTAD. The *J–V* curves are displayed (Figure 8b), and the associated photovoltaic parameters are summarized in Table 3.

The reference PSC with doped Spiro-OMeTAD exhibited a J_{SC} of 23.786 mA cm^{-2}, a V_{OC} of 1007.9 mV, and a fill factor (FF) of 78.8%, resulting in a PCE of about 18.9%. This performance aligns with standard values for our planar perovskite architecture utilizing Spiro-OMeTAD. Among the ZnPc-based devices, **ZnPc-2** gave higher performance, and the device attained a J_{SC} of 22.514 mA cm^{-2}, a V_{OC} of 937.4 mV, and a FF of 75.79%, which corresponds to a PCE of 15.94%, which is lower than that of the Spiro-OMeTAD. The lower V_{OC} obtained with **ZnPc-2**, almost 50 mV lower than that of the Spiro (reference), is due to the slightly upward shif of HOMO level of **ZnPc-2** with the perovskite, causing a large offset [26]. The somewhat diminished J_{SC} for **ZnPc-2** (compared to Spiro) may result from its absorption at a higher wavelength range beyond 700 nm (Q-band absorption effect) [26]. The **ZnPc-1** devices exhibited commendable performance, with a J_{SC} of 21.625 mA cm^{-2}, a V_{OC} of 952.3 mV, and a FF of 74.90% resulting in a PCE of 15.43% with a small reduction in comparison to **ZnPc-2**. The remaining ZnPc derivatives (**ZnPc 3–6**) gave comparatively lower performance (Table 3). The lower device performance correlates with PCEs below 10% for **ZnPc-3 and ZnPc-4** and is even limited for **ZnPc-6**, which is also hypothesized to be due to its inability to form a uniform thin film without holes, and underscores how the molecular design impacts solubility and thus device performance. The trend in device performance follows material characterizations, where **ZnPc-2** (and **ZnPc-1**) showed PL quenching, gave high photocurrents and voltages, while **ZnPc-6**, exhibiting the lowest mobility and inadequate PL quenching, attests to its significant losses in both J_{SC} and V_{OC}. The FFs of the **ZnPc 3–6** devices exhibits low value (often < 60%), presumably attributable to elevated series resistance (resulting from reduced conductivity) and enhanced recombination due to inadequate surface coverage (reduced solubility in chlorobenzene, which is the standard solvent, and molecular aggregation), resulting in shunting channels or inhibiting hole collection [26].

TABLE 2 | Best fit results of the EPR spectra for various ZnPCs 1–6.

HTMs	*N*, spin/mg	g_1	ΔH_{pp1}, Gauss	g_2	ΔH_{pp2}, Gauss	I_1/I_2
ZnPc-1	5.1×10^{14}	2.0025	3.8	2.0028	6.5	1.41
ZnPc-2	1.2×10^{14}	2.0027	4.3	2.0026	7.4	0.40
ZnPc-3	4.5×10^{14}	2.0026	4.3	2.0026	7.3	0.97
ZnPc-4	1.1×10^{15}	2.0026	4.1	2.0029	7.0	1.35
ZnPc-5	5.4×10^{13}	2.0031	5.4	2.0031	6.1	11.50
ZnPc-6	7.2×10^{13}	2.0034	5.8	2.0031	9.4	6.50

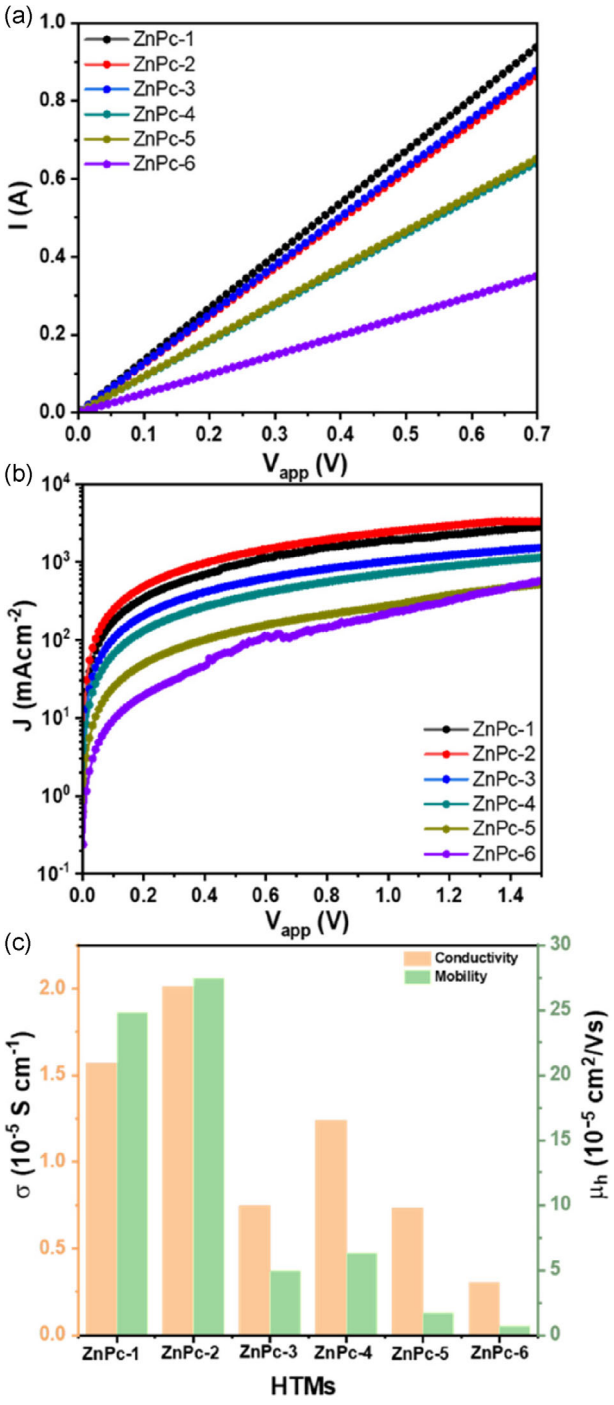

FIGURE 7 | (a) Dark current–voltage characteristics for conductivity measurement with ITO/HTM/Ag, (b) *J–V* curve for hole mobility measurement with device configuration of ITO/PEDOT:PSS/HTM/Ag, and (c) conductivity and mobility summarized values for different ZnPc.

ZnPc-2 and **ZnPc-1** measured competitive performance and with fine-tuning of the design and doping ratio, can push charge transfer and energy alignment for effective PSCs fabrication. The reverse and forward scan *J–V* profiles are obtained to elucidate the hysteresis behavior of each ZnPc-HTM (Figure S23), with the hysteresis indices (HI) presented in Table S2. **ZnPc-1** and **ZnPc-2** showed lower hysteresis values and are comparable to the Spiro-OMeTAD devices.

We evaluated the energy levels of ZnPc in solution form and also complemented the results by theoretical calculation . The HOMO onsets of ZnPc lie approximately between −5.3 and −5.6 eV and show systematic deepening with subsequent fluorination; this can be assigned to molecular quadrupole and orientation effects in the solid state [38–41]. With the HOMO level values and the optical gaps of the ZnPc, we calculated the LUMO value and have sketched an energy level diagram of all ZnPcs with respect to a mixed-cation perovskite valence band maximum (VBM) as reported around −5.8 eV [27]. In this context, **ZnPc-2** exhibits a modest yet positive driving force for hole extraction, which aligns with its pronounced PL quenching, reduced interfacial charge transport resistance, and elevated open-circuit voltage/FF, whereas **ZnPc-5/6** configurations are less advantageous and exhibit less PL quenching and increased interfacial resistance.

The energy level alignment between the VBM of perovskite and HOMO of ZnPc derivatives , are key to understand the impact of fluorination on the hole transfer process (Figure S27). Notwithstanding the deepening of the HOMO, the energy level alignment continues to be favorable for hole transfer from perovskite to ZnPc derivatives. For the HTM, the main parameter is the hole-extraction driving force,

$$\Delta E_{\mathrm{h}} = E_{\mathrm{VBM}}^{\mathrm{PSK}} - E_{\mathrm{HOMO}}^{\mathrm{HTL}}$$

The energy level offset facilitates the interfacial hole transfer. The band offset is nearly negligible for the complete fluorination of ZnPc, which indicates that the entire transfer process will be viable, if not necessarily efficient. The **ZnPc-2** produces significant hole-extraction driving force and strong electron blocking while minimizing a significant energy barrier at the perovskite/HTM interface. This reduces nonradiative recombination, hence decreasing ΔV_{nr} and increasing V_{OC}. This alignment results in consistent PL quenching and reduces interfacial resistance in electrochemical impedance spectroscopy (EIS), leading to enhanced FF and improved MPP stability compared to other ZnPc derivatives.

The EQE and corresponding integrated current density spectra of the ZnPc-based and Spiro-OMeTAD based PSCs are registered to investigate the photoresponsivity (Figure 8c). The EQE magnitude and specific spectral response significantly differ depending on the type of ZnPcs used. The devices with **ZnPc-2** and Spiro-OMeTAD showed similar EQE values at wavelengths ranging from 300 to 650 nm, while the device with other ZnPcs gave a lower EQE value than the device with Spiro-OMeTAD at wavelengths ranging from 650 to 800 nm. Spiro-OMeTAD based PSCs attain the maximum EQE overall, achieving ≈90% in the 450–750 nm spectrum and maintaining above 70% even at 750 nm. Compared to other ZnPCs based PSCs, **ZnPc-2**, exhibits a high EQE of ≈80%–85% in the spectral region of 300–650 nm, while at longer wavelengths it showed a lower EQE value than of Spiro-OMeTAD at wavelengths ranging from 650 to 800 nm. ZnPc exhibiting wavelength-dependent losses, notably reflected in reduced EQE in some spectral regions, particularly at longer wavelengths, due to Q-band absorption. **ZnPc-4** has a marginally reduced EQE plateau, maximum of ≈75%, maintaining a comparatively elevated level in the mid-spectrum while experiencing a more pronounced decline in the near-infrared region. Conversely, the other derivatives exhibit considerable underperformance: **ZnPc-3** attains a modest maximum EQE of

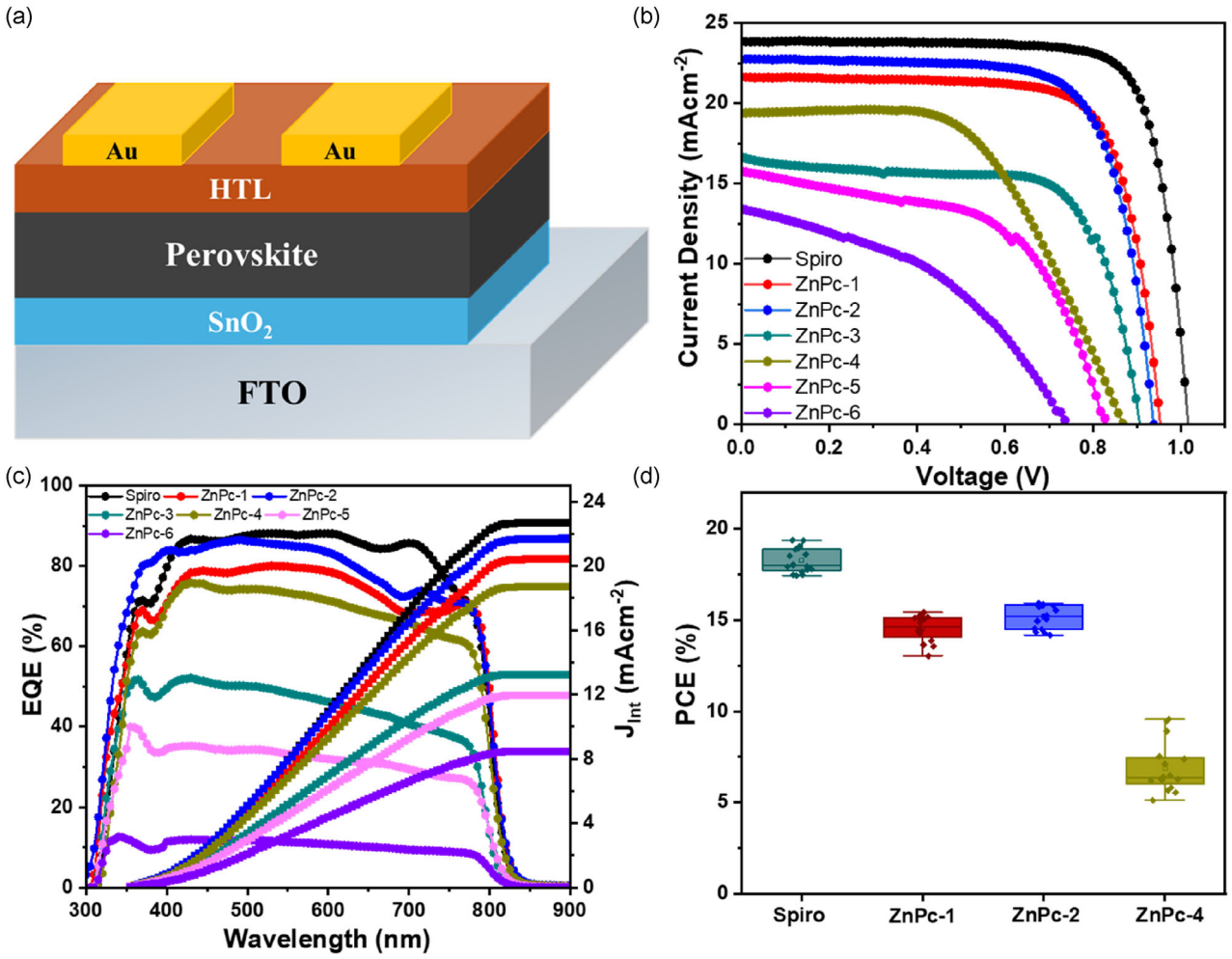

FIGURE 8 | (a) Schematic illustration of the n–i–p device architecture used in this study, (b) *J–V* characteristics of PSCs with **ZnPc1–ZnPc6** and Spiro-OMeTAD, (c) EQE spectra and integrated current densities of the corresponding devices, and (d) statistical distribution of PCE for each HTM.

≈50%–60%, whilst **ZnPc-5** and **ZnPc-6** are markedly inferior, at 40% and below 20%, respectively. The EQE of **ZnPc-5** and **ZnPc-6** is reduced across the wavelengths, signifying a significant reduction in photo response. The primary causes are interfacial recombination due to interface defects and parasitic absorption within the HTM, together with variations in conductivity and surface coverage. The integrated current density values are determined to be 22.69, 21.68, 20.41, 13.24, 18.70, 11.95, and 8.45 mA cm^{-2} for Spiro, **ZnPc-1**, **ZnPc-2**, **ZnPc-3**, **ZnPc-4**, **ZnPc-5**, and **ZnPc-6**, respectively (Figure 8d). The integrated current density of Spiro, **ZnPc-1**, **ZnPc-2**, and **ZnPc-4** aligns with the trend of J_{sc} derived from *J–V* curves. The device statistics are shown for representative ZnPc in Figure 8d.

We use electrochemical impedance spectroscopy to investigate the charge transfer and recombination properties at the perovskite/HTM interfaces. Nyquist plots (–Z″ vs. Z′) for Spiro-OMeTAD, **ZnPc-1**, and **ZnPc-2** based PSCs, recorded at 900 mV under illumination, are presented (Figure 9a). Each device exhibits a singular dominant semicircle, linked to the recombination resistance (R_{rec}) and charge transport resistance (R_{ctr}) within the cell and fitted with the equivalent circuit (Figure S25). At a potential of 700 mV, the Spiro, **ZnPc-1**, and **ZnPc-2** based PSCs have differences in R_{rec} and R_{ctr} values (Figure 9b,c); however, at higher potentials, ZnPc have comparable values to the Spiro-OMeTAD, implying lower charge recombination and mitigating charge recombination at the perovskite/HTM interface, consistent with the observed reduction in V_{OC} loss in **ZnPc-1** and **ZnPc-2** based PSC. In standard interpretation, a larger R_{rec} might indicate reduced recombination rates at the perovskite/HTM interface, which generally correlates with an enhanced V_{OC}. The Nyquist analysis indicates that substituting Spiro-OMeTAD with ZnPc-based HTMs significantly enhances interfacial impedance. The fitted curves and extracted resistance values indicate that **ZnPc-1** has the highest charge–transfer resistance, hindering carrier injection, and the lowest recombination resistance, accelerating loss mechanisms, compared to Spiro. **ZnPc-2** produces intermediate values of R_{ctr} and R_{rec}. The impedance patterns correspond with photovoltaic performance: Spiro-OMeTAD's low interfacial resistance supports its superior FF and photovoltage, while **ZnPc-1**'s increased R_{ctr} results in reduced carrier transport and efficiency. The increased widths of the bigger semicircles for ZnPc devices signify reduced hole-transport kinetics and increased recombination at the perovskite/HTL interface.

The normalized MPP (J_{MPP}) tracking under continuous one-sun illumination in ambient settings (60%–80% RH, room temperature) demonstrates substantial disparities in operational stability across devices based on Spiro-OMeTAD, **ZnPc-1**, and **ZnPc-2** (Figure S26). Within a 24-h timeframe, the **ZnPc-2** based device

TABLE 3 | Photovoltaic devices parameters for different ZnPc1–6 as HTMs.

HTMs	Scan	J_{SC}, mAcm^{-2}	V_{OC}, mV	FF, %	PCE, %
ZnPc-1	RS	21.625	952.3	74.901	15.426
	FS	21.648	947.9	70.337	14.688
ZnPc-2	RS	22.514	934.3	75.788	15.943
	FS	22.783	937.4	72.896	15.545
ZnPc-3	RS	16.685	905.5	69.852	10.554
	FS	15.056	906.9	65.244	8.909
ZnPc-4	RS	19.404	867.8	56.173	9.459
	FS	19.285	859.8	45.371	7.523
ZnPc-5	RS	15.824	829.6	54.776	7.191
	FS	15.866	765.6	42.395	5.151
ZnPc-6	RS	13.409	741.7	41.872	4.165
	FS	7.301	790.4	21.801	1.258
Spiro-OMeTAD	RS	23.786	1007.9	78.799	18.893
	FS	24.158	1007.8	73.046	17.785

maintains roughly 80% of its initial J_{MPP}, surpassing the Spiro-OMeTAD (nearly 60%) and **ZnPc-1** (around 40%) counterparts. **ZnPc-2** demonstrates a transient initial stabilization succeeded by a slow decline, signifying a more stable HTM/perovskite interface and decreased interfacial deterioration. Conversely, **ZnPc-1** exhibits rapid initial degradation and a persistent decrease, indicating limited thin film quality and reduced sustainability. The Spiro-OMeTAD devices exhibit moderate degradation, aligning with established limitations of dopant-induced instability in ambient settings. **ZnPc-2** as a hole transport material improves the operational longevity of PSCs, while also highlights the essential impact of molecular design on performance and long-term stability upon fluorination substitution. . In comparison to **ZnPc-2** and Spiro-OMeTAD, the ZnPc-1-based PSC shows less PL quenching, the highest charge–transfer resistance, and the lowest recombination resistance, suggesting slower hole extraction and higher interfacial recombination. Top-surface view and cross-sectional SEM image show that **ZnPc-1** forms a thinner film (35 nm) that doesn't conform well and has microvoids. In addition, the measured water contact angle is ~82.5°, which is lower than that of **ZnPc-2** (~87.7°). Factors such as a higher number of charge carriers at the interface and quicker moisture absorption due to voids present at the surface accelerating chemical and electrochemical deterioration at the perovskite/HTM interface during unencapsulated MPP tracking. This explains the rapid degradation of **ZnPc-1**. Moreover, ZnPc macrocycles with fewer fluorine atoms can photosensitize O_2 when exposed to light, producing reactive oxygen species, which in turn can degrade the perovskite. The susceptibility to this degradation is reduced by electron-withdrawing substitution in **ZnPc-2**. This, together with a favorable energetic offset and better film uniformity, explains its improved stability. Although the aging of doped Spiro-OMeTAD is caused by hygroscopic dopants, its initial smooth and thicker overlayer provides a better short-term moisture barrier than the microvoids present in **ZnPc-1** film, and Spiro-OMeTAD shows less degradation than

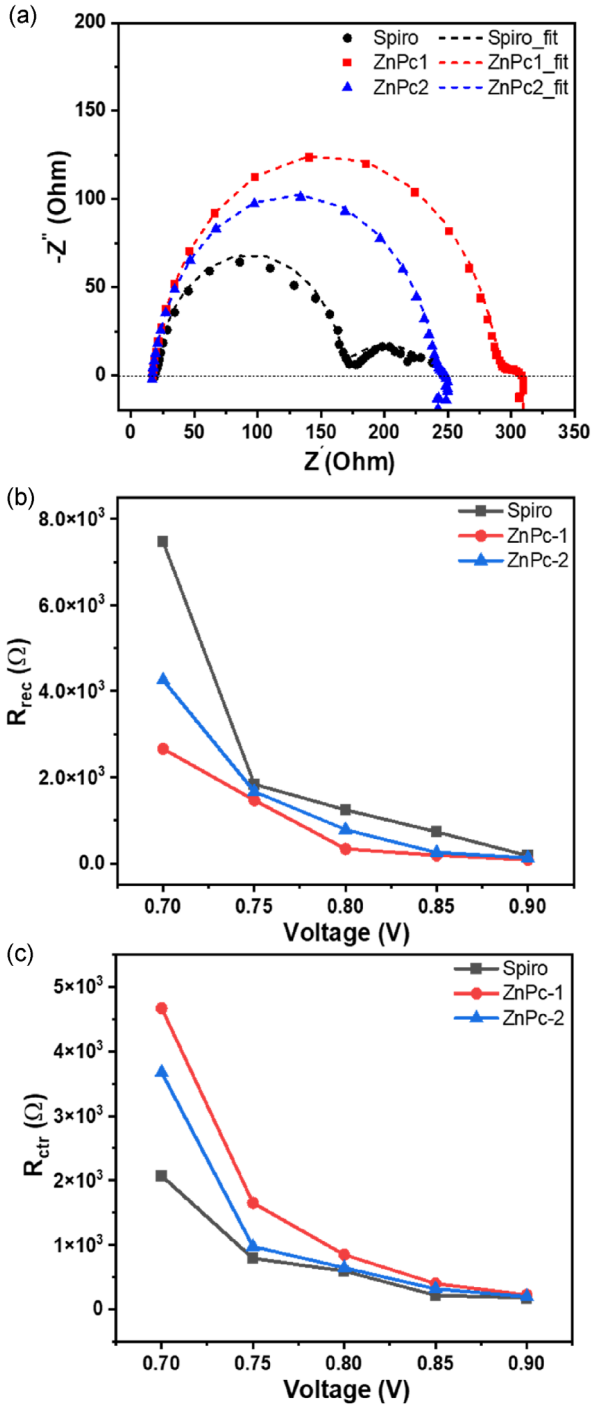

FIGURE 9 | (a) Nyquist plots of PSCs with Spiro-OMeTAD, **ZnPc-1**, and **ZnPc-2** as HTMs, measured under dark conditions at 900 mV bias in the frequency range of 2 MHz to 1 Hz, (b) corresponding charge transfer resistance (R_{ctr}), and (c) recombination resistance (R_{rec}) values extracted by fitting the impedance spectra with an equivalent circuit model.

ZnPc-1 during the first 24 h in ambient air. When optimized p-type dopants (like F_4-TCNQ), and/or interfacial buffers (MoO_3/WO_x, perovskite surface passivation) are used, along with control of thickness and macrocycle orientation, CuPc in PSCs have achieved PCEs ~20%. In contrast, dopant-free, solution-processed ZnPc derivatives usually have PCEs of about 13%–16%, which is in line with our ZnPc-2 results and shows that they are more stable in operation. The comparison of

various phthalocyanines used in PSCs is summarized in Table S3. The difference in performance of PCE is mostly due to device engineering (doping, deposition process, interface passivation, and ultrathin-film orientation control) rather than fundamental limitations of the phthalocyanine core. In this study, we deduce structure–property trends; **ZnPc-2** demonstrates the optimal equilibrium of hole-extraction offset, film quality, and stability. We expect that typical enhancements (p-doping or F_4-TCNQ coevaporation, MoO_3/WO_x capping, and perovskite surface passivation) will raise the PCE of **ZnPc-2** to >20% ranged.

The advantages of fluorine substitution, which enhances ionization energy and hydrophobicity, are dependent on the solution-processability of the HTM on the perovskite. In our solution-processed platform, ZnPc-3,4,5,6 exhibits lower solubility in chlorobenzene (CB) compared to **ZnPc-1** and **2**, resulting in nonuniform, thinner thin films with pinholes (SEM; cross-sections) and subsequently exhibits decreased PL quenching alongside high charge transport resistance (shown by EIS measurements). Introducing THF into the CB solvent enhances solubility but compromises the perovskite/HTM interface, which is consistent with partial surface dissolution and coordination, resulting in reduced V_{OC} and FF compared to that with only CB as a solvent. Thus, an increasing number of substituent groups with fluorine atoms above a moderate threshold is disadvantageous because it impairs film formation and charge transport (due to steric disruption of π–π packing) and, coupled with a greater ΔE_h (from our energy alignment analysis), increases nonradiative losses. **ZnPc-2**, featuring a singular $-O(CH_2)CF_3$ substituent, achieves an ideal balance: (i) a nearly optimal hole-extraction offset favorable to enhanced V_{OC}/FF, (ii) sufficient conductivity/mobility without undue steric hindrance, and (iii) effective coverage using CB as a solvent without the need for THF. Our findings demonstrates why an increased concentration of fluorine does not enhance efficiency within our processing parameters and highlights the functional significance of fluorine in phthalocyanine hole transport layers.

3 | Experimental

3.1 | Materials

PbI_2 (99.999%) was procured from Tokyo Chemical Industry Co. (TCI). Formamidine iodide (FAI), methylammonium iodide (MAI), methylammonium chloride (MACl), and mesoporous materials a dispersion of TiO_2 nanoparticles (30 NRD) was acquired from Greatcell Solar Materials Ltd. Tin(IV) oxide (SnO_2), 15% colloidal in H_2O, was acquired from Fisher Scientific. Chlorobenzene (CB, 99%), isopropanol (IPA, 99.9%), anhydrous dimethyl sulfoxide (DMSO, 99.8%), and *N*,*N*-dimethylformamide (DMF, 99.8%) were acquired from Acros Organics. All chemicals and solvents were acquired from Sigma Aldrich (Merck) and TCI and utilized without additional purification unless specified differently. Microwave-assisted reactions were performed in a Discover SP microwave reactor (CEM Corporation). The purification of the various products by chromatography was carried out using a CombiFlash NextGen 300 system. NMR spectra were recorded on a BRUKER AVANCE NEO 400 spectrometer. UV–visible spectra were recorded using a Perkin-Elmer Lambda 365 spectrophotometer. Fluorescence spectra were recorded using a HORIBA scientific SAS spectrophotometer and for thin film PerkinElmer LS55 was used. Electron paramagnetic resonance (EPR) spectroscopy experiments were made with the help of a Bruker ELEXSYS E500 spectrometer. High-resolution mass spectra were obtained from a Bruker Microflex LRF20 matrix-assisted laser desorption/ionization-time of flight (MALDI-TOF) setup, utilizing dithranol as the matrix. IR spectra were recorded with a Nicolet Impact 400D spectrophotometer. Cyclic voltammetry was performed in a conventional three-electrode cell using a μ-AUTOLAB type III potentiostat/galvanostat at 298 K in DMF and deaerated sample solutions containing 0.10 M tetrabutylammonium hexafluorophosphate ($TBAPF_6$) as the supporting electrolyte. Platinum served as the working electrode, $Ag/AgNO_3$ (0.01 M in benzonitrile) as the reference electrode, and platinum as the wire counter electrode. The ferrocene/ferrocenium redox couple was employed as an internal standard for all measurements.

3.2 | Synthesis of ZnPc-2

226 mg (1 mmol) of phthalonitrile **7**, 552.70 mg (3 mmol) of 4-*tert*-butylphthalonitrile, and 367 mg (2 mmol) of $Zn(OAc)_2$ in 2 mL of DMAE and two drops of DBN under an inert atmosphere were stirred at 140°C for 1 h under microwave irradiation (71 W). After cooling to room temperature, the blue reaction mixture was concentrated under reduced pressure and purified by column chromatography (hexane/dioxane, 85:15), affording **ZnPc-2** as a blue solid (53 mg, 6% yield). ^{1}H-NMR (400 MHz, THF-d_8): (mixture of regioisomers), $\delta = 9.59$–9.48 (m, 3H), 9.44–9.28 (m, 4H), 9.02–8.93 (m, 1H), 8.35–8.28 (m, 3H), 7.87–7.76 (m, 1H), 5.23–5.14 (m, 2H), 1.83–1.79 (m, 27H). ^{19}F-NMR (400 MHz, THF-d_8): (mixture of regioisomers), $\delta = -74.68$ to -74.58 (m). HR-MALDI-TOF (dithranol): *m/z* for $C_{46}H_{41}F_{12}N_8OZn$: calcd. 842.2591 [M^+]; found, 842.2520. UV–vis (DMF) λ_{max}/nm (log ε): 675 (5.47), 608 (4.68), 350 (4.89). FT-IR: ν_{max}/cm^{-1}: 3434, 2957, 2904, 2867, 1613, 1458, 1393, 1364, 1332, 1283, 1257, 1236, 1165, 1131, 1091, 1047, 975, 923, 862, 830, 746, 672, 600, 527, 443.

3.3 | Synthesis of ZnPc-3

216 mg (0.96 mmol) of phthalonitrile **7**, and 87.68 mg (0.48 mmol) of $Zn(OAc)_2$ in 500 μL of DMAE and one drop of DBN under an inert atmosphere were subjected to microwave irradiation (140°C, 1 h, 71 W). The blue mixture was cooled to room temperature, concentrated under reduced pressure, and purified by flash column chromatography (hexane:dioxane, 60:40), affording **ZnPc-3** (125 mg, 54%) as a blue solid. ^{1}H-NMR (400 MHz, THF-d_8): (mixture of regioisomers), $\delta = 9.08$–8.95 (m, 4H), 8.68–8.55 (m, 4H), 7.78–7.68 (m, 4H), 5.20–5.10 (m, 8H). ^{19}F-NMR (400 MHz, THF-d_8): (mixture of regioisomers), $\delta = -74.61$ to -74.49 (m). HR-MALDI-TOF (dithranol): *m/z* for $C_{40}H_{20}F_{12}N_8O_4Zn$: calcd. 968.0671 [$M^+$]; found, 968.0779. UV–vis (DMF) λ_{max}/nm (log ε): 671 (5.27), 607 (4.54), 350 (4.84). FT-IR: ν_{max}/cm^{-1}: 3441, 2949, 1611, 1490, 1457, 1238, 1165, 1122, 1099, 1079, 1039, 973, 860, 828, 744, 673, 569, 518, 436.

3.4 | Synthesis of ZnPc-4

50 mg (0.26 mmol) of phthalonitrile **8**, 188 mg (1.02 mmol) of 4-*tert*-butylphthalonitrile, 93.55 mg (0.51 mmol) of $Zn(OAc)_2$, and one drop of DBN were dissolved in 500 μL of DMAE under an

inert atmosphere. The reaction mixture was heated under microwave irradiation (140°C, 1 h, 71 W). Upon completion, the reaction mixture was cooled to room temperature, evaporated under reduced pressure, and subjected to flash column chromatography (hexane/dioxane, 90:10), yielding **ZnPc-4** as a blue solid (30 mg, 15%). ^{1}H-NMR (400 MHz, THF-d_8): (mixture of regioisomers), $\delta = 9.72–9.66$ (m, 1H), 9.58–9.48 (m, 4H), 9.40–9.29 (m, 3H), 8.46–8.40 (m, 1H), 8.37–8.29 (m, 3H), 1.80–1.85 (m, 27H). ^{19}F-NMR (400 MHz, THF-d_8): (mixture of regioisomers), $\delta = -61.43 - -61.25$ (m). HR-MALDI-TOF (dithranol): m/z for $C_{45}H_{39}F_3N_8Zn$: calcd. 812.2543 [M^+]; found, 812.2538. UV–vis (DMF) λ_{max}/nm (log ε): 680 (4.96) 669 (4.93), 607 (4.25), 350 (4.53). FT-IR: ν_{max}/cm^{-1}: 2957, 2903, 2866, 1723, 1660, 1615, 1485, 1364, 1313, 1263, 1165, 1123, 1093, 1059, 1042, 922, 829, 762, 745, 694, 672, 610, 569, 526, 443.

3.5 | Synthesis of ZnPc-5

Phthalonitrile **8** (216 mg, 0.96 mmol), 4-*tert*-butylphthalonitrile (21.92 mg, 0.12 mmol), $Zn(OAc)_2$ (44 mg, 0.24 mmol), and one drop of DBN were dissolved in 500 µL of DMAE under a nitrogen atmosphere. The reaction was carried out under microwave irradiation at 140°C for 1 h. Upon completion, the reaction mixture was allowed to cool to room temperature, then concentrated under reduced pressure. The residue was purified by flash column chromatography on silica gel using a mixture of hexane and dioxane (75:25) as eluent, affording **ZnPc-5** as a blue solid (12 mg, 12%). ^{1}H-NMR (400 MHz, THF-d_8): (mixture of regioisomers), $\delta = 9.47–8.94$ (m, 8H), 8.58–8.28 (m, 4H), 1.97–1.95 (m, 9H). ^{19}F-NMR (400 MHz, THF-d_8): (mixture of regioisomers), $\delta = -61.47$ to -61.27 (m). HR-MALDI-TOF (dithranol): m/z for $C_{39}H_{21}F_9N_8Zn$: calcd. 836.1119 [M^+]; found, 836.1092. UV–vis (DMF) λ_{max}/nm (log ε): 676 (4.85), 665 (4.85), 604 (4.14), 373 (4.29), 334 (4.29). FT-IR: ν_{max}/cm^{-1}: 2958, 2925, 2855, 1669, 1623, 1483, 1398, 1346, 1266, 1168, 1125, 1091, 1073, 1041, 916, 836, 745, 676, 464.

3.6 | Synthesis of ZnPc-6

200 mg (1.02 mmol) of **8** and 93.55 mg (0.51 mmol) of $Zn(OAc)_2$ in 500 µL of DMAE and one drop of DBN under an inert atmosphere. The reaction was performed under microwave irradiation at 140°C for 1 h with 71 W. The blue mixture was cooled at room temperature, concentrated under vacuum, and purified by column chromatography (hexane: dioxane/70:30), yielding 99 mg of **ZnPc-6** (46%) as a blue solid. ^{1}H-NMR (400 MHz, THF-d_8): (mixture of regioisomers), $\delta = 9.41–9.29$ (m, 4H), 9.21–9.08 (m, 4H), 8.54–8.39 (m, 4H). ^{19}F-NMR (400 MHz, THF-d_8): (mixture of regioisomers), $\delta = -61.56$ to -61.46 (m). HR-MALDI-TOF (dithranol): m/z for $C_{36}H_{12}F_{12}N_8Zn$: calcd. 848.0297 [M^+]; found, 848.0546. UV–vis (DMF) λ_{max}/nm (log ε): 671 (5.33), 604 (4.55), 385 (4.63), 329 (4.64). FT-IR: ν_{max}/cm^{-1}: 2961, 2926, 2854, 1719, 1666, 1623, 1481, 1433, 1315, 1265, 1167, 1127, 1077, 1041, 915, 840, 797, 770, 747, 735, 699, 666, 510.

3.7 | Device Fabrication

FTO-coated glass substrates (TEC-15) were dried using compressed air after being washed with Helmanex, deionized water, acetone, and isopropanol. These substrates were treated with UV ozone for 30 min before usage. Spray pyrolysis at 500°C using a titanium(IV) diisopropoxide bis(acetylacetonate) precursor solution (75% in 2-propanol) diluted in ethanol at a 1/19 ratio resulted in a compact TiO_2 blocking layer on the FTO substrates. The substrates were spin-coated with a colloidal SnO_2 solution (SnO_2:H_2O = 1:4) at 5000 rpm for 30 s, then annealed at 150°C for 20 min in air. The substrate was moved to an argon-filled glovebox and annealed at 150°C for 20 min. To create the perovskite, the $Cs_{0.05}FA_{0.9}MA_{0.05}PbI_3$ solution was spin-coated on top of the SnO_2 layer using an antisolvent-assisted two-step technique. The process involved spinning at 1000 rpm for 10 s, then 6000 rpm for 30 s, followed by an annealing at 100°C for 1 h and 150°C for 10 min. Next, a 10 mM solution of ZnPc 1–6 as HTM in chlorobenzene with minor addition of LiTFSI (4.2 µL) and t-BP (7.4 µL) as dopant, was prepared and spin-coated onto the perovskite layer at 4000 rpm for 30 s at room temperature. To fabricate the reference solar cells, Spiro-OMeTAD was dissolved in 1 mL of chlorobenzene, followed by LiTFSI solution (28.5 µL from 520 mg mL^{-1} in acetonitrile) and *t*-BP (28.5 µL) doping. The cells were then spin-coated at 4000 rpm for 30 s. The solar cell was completed with a gold electrode (~70 nm thick) deposited by thermal evaporation under low vacuum conditions (below 4.6×10^{-6} Torr) at a rate of less than 1 Å s^{-1}.

3.8 | Thin Film and Devices Characterization

The surface microstructure was evaluated utilizing field emission scanning electron microscopy (Hitachi S-4800). Current-density (J–V) curves were obtained utilizing a Keithley 2400 source meter and a Newport ORIEL AAA solar simulator under 100 mW cm^2 (AM1.5) irradiation. Calibration was conducted using an NREL-certified monocrystalline silicon solar cell. The photocurrent was measured at a scan rate of 100 mV s^{-1} (presweep delay: 10 s) utilizing a 0.09 cm^2 black metal mask as the active region. The EQE spectrum was obtained utilizing a 150 W xenon light and a Bentham PVE300 motorized 1/4 m monochromator. EIS was conducted utilizing a Biologic SP-300 impedance analyzer across a frequency range of 2 MHz to 1 Hz under an AC signal within a Faraday chamber, with data analysis executed via EC-Lab software.

3.9 | Computational Details

DFT calculations were performed by using the Gaussian 16 program [42] with exchange-correlation functional TPSSh [43, 44] together with 6-311G* basis set [45]. The frequencies were calculated to verify that the optimized structures are energy minima. The Cartesian coordinates of the optimized structure are provided in SI. The electrostatic potential figures were calculated using the GaussView program [46].

4 | Conclusion

We developed and validated a series of zinc phthalocyanine derivatives as hole transport materials , where the zinc phthalocyanine with three *tert*-butyl groups and a trifluoroethoxy group gave competitive results, which stems from its aligned energy level and higher solubility. The solar cells fabricated thereof

measured a power conversion efficiency of 15.94%, inching toward the standard Spiro-OMeTAD , while consuming a significantly lower amount of materials. The peripheral substituents allow **ZnPc-2** to fulfill the essential criteria for an effective hole transport material and possess intrinsic hole mobility akin to doped Spiro-OMeTAD. **ZnPc-2** preserved about 80% of its initial output after 24 h of operation in ambient conditions (60%–80% humidity), while Spiro-OMeTAD devices deteriorated to ≈50% during the same duration. The inherent stability induced through fluorination, and its mild interfacial resistance mitigates recombination losses. Our findings add to the increasing evidence that molecularly designed hole transport materials such as **ZnPc-2** can address the challenges in perovskite photovoltaics, and with alternative derivatives with advantageous substituents.

Acknowledgements

This work received funding from the Spanish Ministry of Science and Innovation INTERACTION {PID2021-129085OB-I00}, PID2024-163070OB-I00 and PID2024-155562-I00. The authors also wish to thank the European Regional Development Fund "A Way to Make Europe" and the Spanish Ministerio de Ciencia e Innovación/Agencia Estatal de Investigación (PID2024-155430OB-I00 to Á.S.-S) and the Generalitat Valenciana (CIPROM/2021/059 and MFA/2022/028 to Á.S.-S.) for funding. E.R. thanks Generalitat de Catalunya for an ICREA Academia grant, and computer resources, technical expertise, and assistance provided by the CSUC.

Funding

This work was supported by Ministerio de Ciencia e Innovación (PID2024-155562-I00, PID2024-155430OB-I00, PID2021-129085OB-I00 and PID2024-155562-I00), Agència Valenciana de la Innovació (CIPROM/2021/059 and MFA/2022/028).

Conflicts of Interest

The authors declare no conflicts of interest.

Data Availability Statement

The data that support the findings of this study are available from the corresponding author upon reasonable request.

References

1. L. Shen, P. Song, L. Zheng, et al., "Ion-Diffusion Management Enables All-Interface Defect Passivation of Perovskite Solar Cells," *Advanced Materials* 35, no. 39 (2023): 2301624.

2. H. Zhang, S. Zhang, X. Ji, et al., "Formamidinium Lead Iodide-Based Inverted Perovskite Solar Cells with Efficiency over 25% Enabled by An Amphiphilic Molecular Hole-Transporter," *Angewandte Chemie International Edition* 136 (2024): e202401260.

3. J. Zhou, L. Tan, Y. Liu, et al., "Highly Efficient and Stable Perovskite Solar Cells via a Multifunctional Hole Transporting Material," *Joule* 8 (2024):1691–1706.

4. P. Culık, J. Kouril, A. Prech, et al., "Design and Cost Analysis of 100 MW Perovskite Solar Panel Manufacturing Process in Different Locations," *ACS Energy Letters* 2022) : 3039–3044.

5. H. C. Weerasinghe, N. Macadam, J.-E. Kim, et al., "The First Demonstration of Entirely Roll-to-roll Fabricated Perovskite Solar Cell Modules under Ambient Room Conditions," *Nature Communications* 15 (2024): 1656.

6. D. Bi, W. Tress, M. I. Dar, et al., "Efficient Luminescent Solar Cells Based on Tailored Mixed-Cation Perovskites," *Science Advances* 2, no. 1 (2024): e1501170.

7. K. M. Anoop and T. N. Ahipa, "Hole-Transport Materials for Perovskite Solar Cells," *Solar Energy* 263 (2023): 111937.

8. X. Yin, Z. Song, Z. Li, and W. Tang, "Toward Ideal Hole Transport Materials: A Review on Recent Progress in Dopant-Free Hole Transport Materials for Fabricating Efficient and Stable Perovskite Solar Cells," *Energy & Environmental Science* 13, no. 11 (2020): 4057–4086.

9. B. Yadagiri, T. H. Chowdhury, Y. He, R. Kaneko, A. Islam, and S. P. Singh, "Pyridyl-Functionalized Spiro[Fluorene– Xanthene] as a Dopant-Free Hole-Transport Material for Stable Perovskite Solar Cells," *Materials Chemistry Frontiers* 5, no. 19 (2021): 7276–7285.

10. B. Yadagiri, K. Narayanaswamy, T. H. Chowdhury, A. Islam, V. Gupta, and S. P. Singh, "Application of Small Molecules Based on a Dithienogermole Core in Bulk Heterojunction Organic Solar Cells and Perovskite Solar Cells," *Materials Chemistry Frontiers* 4, no. 7 (2020): 2168–2175.

11. P. Mahajan, B. Padha, S. Verma, et al., "Review of Current Progress in Hole-Transporting Materials for Perovskite Solar Cells," *Journal of Energy Chemistry* 68 (2022): 330–386.

12. P. Murugan, T. Hu, X. Hu, and Y. Chen, "Advancements in Organic Small Molecule Hole-Transporting Materials for Perovskite Solar Cells: Past and Future," *Journal of Materials Chemistry A* 10 (2022): 5044–5081.

13. B. G. Krishna, D. S. Ghosh, and S. Tiwari, "Hole and Electron Transport Materials: A Review on Recent Progress in Organic Charge Transport Materials for Efficient, Stable, and Scalable Perovskite Solar Cells," *Chemistry of Inorganic Materials* 1 (2023): 100026.

14. M. Jeong, I. W. Choi, K. Yim, et al., "Large-Area Perovskite Solar Cells Employing Spiro-Naph Hole Transport Material," *Nature Photonics* 16, no. 2 (2022): 119–125.

15. E. Molins, C. Miravitlles, E. Espinosa, and M. Ballester, "1,10,3,30,6,60,8,8-Octachloro-9,9-bifluorenylidene and Perchloro-9,9-bifluorenylidene, Two Exceedingly Twisted Ethylenes," *The Journal of Organic Chemistry* 67, no. 21 (2002): 7175–7178.

16. Q. Hu, E. Rezaee, W. Xu, et al., "Dual Defect-Passivation using Phthalocyanine for Enhanced Efficiency and Stability of Perovskite Solar Cells," *Small* 17, no. 1 (2021): 2005216.

17. J. Cao, C. Li, X. Lv, et al., "Efficient Grain Boundary Suture by Low-Cost Tetra-Ammonium Zinc Phthalocyanine for Stable Perovskite Solar Cells with Expanded Photoresponse," *Journal of the American Chemical Society* 140, no. 37 (2018): 11577–11580.

18. H. Kim, K. S. Lee, M. J. Paik, et al., "Polymethyl Methacrylate as an Interlayer between the Halide Perovskite and Copper Phthalocyanine Layers for Stable and Efficient Perovskite Solar Cells," *Advanced Functional Materials* 32, no. 13 (2022): 2110473.

19. D. Molina, J. Follana-Berná, and Á. Sastre-Santos, "Phthalocyanines, Porphyrins and other Porphyrinoids as Components of Perovskite Solar Cells," *Journal of Materials Chemistry C* 11 (2023): 7885–7919.

20. M. Urbani, G. de la Torre, M. K. Nazeeruddin, and T. Torres, "Phthalocyanines and Porphyrinoid Analogues as Hole- and Electron-Transporting Materials for Perovskite Solar Cells," *Chemical Society Reviews* 48 (2019): 2738–2766.

21. Z. Yu, L. Wang, X. Mu, et al., "Intramolecular Electric Field Construction in Metal Phthalocyanine as Dopant-Free Hole Transporting Material for Stable Perovskite Solar Cells with >21% Efficiency," *Angewandte Chemie International Edition* 60 (2021): 6294–6299.

22. F. Javier Ramos, M. Ince, M. Urbani, et al., "Non-Aggregated Zn(II) octa(2,6-Diphenylphenoxy) Phthalocyanine as a Hole Transporting Material for Efficient Perovskite Solar Cells," *Dalton Transactions* 44 (2015): 10847–10851.

23. Y. C. Kim, T.-Y. Yang, N. J. Jeon, et al., "Engineering Interface Structures between Lead Halide Perovskite and Copper Phthalocyanine for Efficient and Stable Perovskite Solar Cells," *Energy & Environmental Science* 10 (2017): 2109–2116.

24. T. Duong, J. Peng, D. Walter, et al., "Perovskite Solar Cells Employing Copper Phthalocyanine Hole-Transport Material with an Efficiency over 20% and Excellent Thermal Stability," *ACS Energy Letters* 3, no. 10 (2018): 2441–2448.

25. M. Pegu, D. Molina, M. J. Álvaro-Martins, et al., "Dimers of Diethynyl-Conjugated Zinc-Phthalocyanine as Hole Selective Layers for Perovskite Solar Cell Fabrication," *Journal of Materials Chemistry C* 10 (2022): 11975–11982.

26. A. Hernandez, N. H. Hemasiri, S. Kazim, J. Ortiz, S. Ahmad, and Á. Sastre-Santos, "Fluorinated- and non-Fluorinated-Diarylamine-Zn(II) and Cu(II) Phthalocyanines as Symmetrical vs. Asymmetrical Hole Selective Materials," *Journal of Materials Chemistry C* 11 (2023): 8243–8253.

27. M. Gassara, J. Garcés-Garcés, L. Lezama, et al., "Dopant-Free Tert-Butyl Zn(II) Phthalocyanines: the Impact of Substitution on their Photophysical Properties and their Role in Perovskite Solar Cells," *Journal of Materials Chemistry C* 13 (2025): 1704–1712.

28. M. Jeong, I. W. Choi, E. M. Go, et al., "Stable Perovskite Solar Cells with Efficiency Exceeding 24.8% and 0.3-V Voltage Loss," *Science* 369 (2020): 1615–1620.

29. A. Ghaderian, M. Pegu, N. H. Hemasiri, P. Huang, S. Ahmad, and S. Kazim, "The Impact of Fluorine Atoms on a Triphenylamine-Based Dopant-Free Hole-Selective Layer for Perovskite Solar Cells," *Journal of Materials Chemistry C* 10 (2022): 476–484.

30. G. Winter, H. Heckmann, P. Haisch, et al., "Study of Substituent Effects on the Photoconductivity of Soluble 2,(3)- and 1,(4)-Substituted Phthalocyaninato- and Naphthalocyaninatotitanium(IV) Oxides," *Journal of the American Chemical Society* 120 (1998): 11663–11673.

31. G. Pawlowski and M. Hanack, "A Convenient Synthesis of Trifluoromethyl Substituted Pthalocyanines," *Synthetic Communications* 11 (1981): 351.

32. S. Gaspard and P. Maillard, "Structure des Phtalocyanines Tetra Tertio-Butylees: Mecanisme de la Synthesis," *Tetrahedron* 43 (1987): 1083.

33. A. Ogunsipe, D. Maree, and T. Nyokong, "Solvent Effects on the Photochemical and Fluorescence Properties of Zinc Phthalocyanine Derivatives," *Journal of Molecular Structure* 650 (2003): 131–140.

34. L. Calio, J. Follana-Berna, S. Kazim, et al., "Cu(II) and Zn(II) Based Phthalocyanines as Hole Selective Layers for Perovskite Solar Cells," *Sustainable Energy Fuels* 1 (2017): 2071–2077.

35. Y. Cao, Y. Li, T. Morrissey, et al., "Dopant-Free Molecular Hole Transport Material that Mediates a 20% Power Conversion Efficiency in a Perovskite Solar Cell," *Energy & Environmental Science* 12 (2019): 3502–3507.

36. T. Niu, W. Zhu, Y. Zhang, et al., "D-A-π-A-D-type Dopant-free Hole Transport Material for Low-Cost, Efficient, and Stable Perovskite Solar cells," *Joule* 5 (2021): 249–269.

37. N. H. Hemasiri, L. Calio, M. Pegu, S. Kazim, and S. Ahmad, "Molecular Interface Engineering via Triazatruxene-Based Moieties/NiOx as Hole-Selective Bilayers in Perovskite Solar Cells for Reliability," *Solar RRL* 6 (2022): 2100793.

38. E. Oleiki, S. Javaid, and G. Lee, "Impact of fluorination on the energy level alignment of an FnZnPc/MAPbI3 interface," *Nanoscale Advances* 4 (2022): 5070–5076.

39. M. Schwarze, K. Schellhammer, K. Ortstein, et al., "Impact of Molecular Quadrupole Moments on the Energy Levels at Organic Heterojunctions," *Nature Communications* 10 (2019): 2466.

40. Y. Uemura, S. A. Abd-Rahman, S. Yanagisawa, and H. Yoshida, "Quantitative Analysis of the Electrostatic and Electronic Polarization Energies in Molecularly Mixed Films of Organic Semiconductors," *Physical Review B* 102 (2020): 125302.

41. Ch. Li, S. Dogan,Y. Li, et al., "Mitigating VOC Loss in Single-Junction and Four-Terminal Tandem Perovskite/Si Photovoltaics with D-A Phthalocyanines Layers," *Advanced Energy Materials* 15 (2025): 2402856.

42. M. J. Frisch, G. W. Trucks, et al., Gaussian 16, Revision C.01 (Gaussian, Inc., 2016).

43. J. M. Tao, J. P. Perdew, V. N. Staroverov, and G. E. Scuseria, "Climbing the Density Functional Ladder: Nonempirical Meta–Generalized Gradient Approximation Designed for Molecules and Solids," *Physical Review Letters* 91 (2003): 146401.

44. V. N. Staroverov, G. E. Scuseria, J. Tao, and J. P. Perdew, "Comparative Assessment of a New Nonempirical Density Functional: Molecules and Hydrogen-Bonded Complexes," *The Journal of Chemical Physics* 119 (2003): 12129.

45. A. D. McLean and G. S. Chandler, "Contracted Gaussian Basis sets for Molecular Calculations. I. Second Row Atoms, Z=11-18," *The Journal of Chemical Physics* 72 (1980): 5639–5648.

46. R. Dennington, T. A. Keith, and J. M. Millam, GaussView, Version 6.1 (Semichem Inc., 2016).

Supporting Information

Additional supporting information can be found online in the Supporting Information section. **Supporting Fig. S1:** ^{1}H-NMR of **ZnPc-2** in THF-d_8. **Supporting Fig. S2:** ^{1}H-NMR of **ZnPc-3** in THF-d_8. **Supporting Fig. S3:** ^{1}H-NMR of **ZnPc-4** in THF-d_8. **Supporting Fig. S4:** ^{1}H-NMR of **ZnPc-5** in THF-d_8. **Supporting Fig. S5:** ^{1}H-NMR of **ZnPc-6** in THF-d_8. **Supporting Fig. S6:** ^{19}F-NMR of **ZnPcs 2-6** in THF-d_8. **Supporting Fig. S7:** Proton decoupled ^{19}F-NMR of **ZnPcs 2-6** in THF-d_8. **Supporting Fig. S8:** Cyclic voltammogram of **ZnPcs 1-6** in DMF. **Supporting Fig. S9:** Normalized UV–Vis absorption and fluorescence spectra of **ZnPc-1** in DMF. **Supporting Fig. S10:** Normalized UV–Vis absorption and fluorescence spectra of **ZnPc-2** in DMF. **Supporting Fig. S11:** Normalized UV–Vis absorption and fluorescence spectra of **ZnPc-3** in DMF. **Supporting Fig. S12:** Normalized UV–Vis absorption and fluorescence spectra of **ZnPc-4** in DMF. **Supporting Fig. S13:** Normalized UV–Vis absorption and fluorescence spectra of **ZnPc-5** in DMF. **Supporting Fig. S14:** Normalized UV–Vis absorption and fluorescence spectra of **ZnPc-6** in DMF. **Supporting Fig. S15:** HR-MALDI-TOF spectrum of **ZnPc-2**. **Supporting Fig. S16:** HR-MALDI-TOF spectrum of **ZnPc-3**. **Supporting Fig. S17:** HR-MALDI-TOF spectrum of **ZnPc-4**. **Supporting Fig. S18:** HR-MALDI-TOF spectrum of **ZnPc-5**. **Supporting Fig. S19:** HR-MALDI-TOF spectrum of **ZnPc-6**. **Supporting Fig. S20:** FT-IR spectrum of **ZnPc-2-6**. **Supporting Fig. S21:** Visual image of the solubility ZnPc derivatives (ZnPc1–ZnPc6) in chlorobenzene. The top row shows the initial dispersion of each compound in the solvent, while the bottom row displays the resulting homogeneous solutions after adding a small amount of THF. The solubility among the derivatives arises from variations in peripheral substituents, influencing solution processability and film uniformity for photovoltaic applications. **Supporting Fig. S22:** Cross-sectional SEM images of PSCs with ZnPc1–ZnPc6 as hole transport layers (HTLs): (a) ZnPc1, (b) ZnPc2, (c) ZnPc3, (d) ZnPc4, (e) ZnPc5, and (f) ZnPc6. The HTL thicknesses, are indicated in the respective images. **Supporting Fig. S23:** Current density–voltage (J–V) characteristics of PSCs incorporating ZnPc1–ZnPc6 as hole transport materials, measured under AM 1.5G illumination (100 mW cm^{-2}). The dashed lines represent the forward scan, and the solid lines correspond to the reverse scan. **Supporting Fig. S24:** Statistical distribution of photovoltaic parameters—(a) short-circuit current density (J_{SC}), (b) open-circuit voltage (V_{OC}), and (c) FF—for PSCs with Spiro-OMeTAD, ZnPc-1, ZnPc-2, ZnPc-4 as hole transport materials. **Supporting Fig. S25:** EIS Nyquist plots of PSCs under illumination at an applied bias from 700 mV to 900 mV and frequency range from 2 MHz – 1 Hz: (a) Spiro-OMeTAD, (b) ZnPc-1, and (c) ZnPc-2. **Supporting Fig. S26:** MPP tracking of PSCs with Spiro-OMeTAD, ZnPc1, and ZnPc2 as hole transport

materials under one-sun illumination in ambient conditions (~60-80% relative humidity, room temperature). **Supporting Fig. S27:** Energy-level diagram of the n-i-p device stack FTO/SnO_2/Perovskite/ZnPc/Au. **Supporting Table S1:** Calculated values of conductivity and hole mobility data of ZnPc HTMs. **Supporting Table S2:** Photovoltaic devices parameters for different ZnPc as HTMs. **Supporting Table S3:** Comparative table of phthalocyanines employed as HTM in PSCs.